



Article

# Measurement of the Heat Transfer Properties of Carbon Fabrics via Infrared Thermal Mapping

Phillip Kearney<sup>1,2,\*</sup>, Constantina Lekakou<sup>1,\*</sup>  and Stephen Belcher<sup>2</sup>

<sup>1</sup> Department of Mechanical Engineering Sciences, University of Surrey, Guildford GU2 7XH, UK

<sup>2</sup> McLaren Composites Technology Centre, McLaren Automotive Limited, Sheffield S60 5XA, UK; stephen.belcher@mclaren.com

\* Correspondence: p.p.kearney@surrey.ac.uk (P.K.); c.lekakou@surrey.ac.uk (C.L.)

**Abstract:** The aim of this paper is to determine the heat transfer properties of biaxial carbon fabrics of different architectures, including non-crimp stitch bonded fabrics, plain, twill and satin woven fabrics. The specific heat capacity was determined via DSC (differential scanning calorimetry). A novel method of numerical analysis of temperature maps from a video using a high-resolution thermal camera is investigated for the measurement of the in-plane and transverse thermal diffusivity and conductivity. The determined thermal conductivity parallel to the fibers of a non-crimp stitch bonded fabric agrees well with the theoretical value calculated employing the rule of mixtures. The presence of voids due to the yarn crossover regions in woven fabrics leads to a reduced value of transverse thermal conductivity, especially in the single ply measurements of this study.

**Keywords:** thermal conductivity; specific heat capacity; woven carbon fabrics; non-crimp stitch bonded fabric; clayton model



**Citation:** Kearney, P.; Lekakou, C.; Belcher, S. Measurement of the Heat Transfer Properties of Carbon Fabrics via Infrared Thermal Mapping. *J. Compos. Sci.* **2022**, *6*, 155. <https://doi.org/10.3390/jcs6060155>

Academic Editor: Francesco Tornabene

Received: 8 April 2022  
Accepted: 24 May 2022  
Published: 25 May 2022

**Publisher's Note:** MDPI stays neutral with regard to jurisdictional claims in published maps and institutional affiliations.



**Copyright:** © 2022 by the authors. Licensee MDPI, Basel, Switzerland. This article is an open access article distributed under the terms and conditions of the Creative Commons Attribution (CC BY) license (<https://creativecommons.org/licenses/by/4.0/>).

## 1. Introduction

Heat transfer plays an important role in all stages of composite manufacturing. Heating in preforming is used to melt the thermoplastic matrix or binder so the fabric can be deformed and the layers consolidated [1,2] and also cure the adhesive binder for thermosetting binders [3,4]. Preforming takes place in single (SDF) [5] or double diaphragm forming (DDF) [6,7] or matched tool forming [8]. Mainstream composite manufacturing techniques [9] include autoclave processing [9], resin transfer molding (RTM) [10,11], vacuum-assisted resin infusion (VARI) [12], automated fiber placement (AFP) [13–15], thermoforming [16,17] and pultrusion [18,19]. Controlled heating is used in all techniques in combination with pressure or vacuum to reduce the matrix viscosity to facilitate resin flow, impregnation or bleeding and layer consolidation as well as to effect solidification via curing for reacting resins, especially thermosets, or cooling for thermoplastic matrices. Product design and process optimization in composite manufacturing is usually conducted via computer simulations in which the heat transfer equation is of particular significance.

The thermal properties of the composite material and the contact resistance at interfaces [20] are key properties in the heat transfer equation that need to be measured and inputted in the computer algorithms. The rule of mixtures or modifications could be used to predict the density and specific heat capacity of a composite material [21,22], both of which are isotropic properties. The specific heat capacity is also measured using differential scanning calorimetry (DSC) [21].

However, it is more difficult to determine the thermal conductivity which is a property depending on the fiber direction or the direction of nano-reinforcements for particulates with an aspect ratio, such as carbon nanotubes, nanofibers and graphene or graphene oxide which may be either randomly oriented in usual mixing, casting, coating via doctor blade or spraying techniques [23–25] or oriented via electrophoresis [26] or electrospinning [27], for example. For unidirectional reinforcements, the rule of mixtures may be used to predict the

thermal conductivity in the direction parallel to the fibers [28]. As heat transfer is dominant through the laminate thickness, the thermal conductivity in the direction transverse to the fibers is critical. It can be predicted by the harmonic mean [28] also known as the inverse rule of mixtures, but that indicates the lower bound on the composite conductivity [29,30]. The next best constitutive relation for the thermal conductivity of a composite transverse to the fibers,  $k_{c,t}$ , is given by Clayton's model [31,32]:

$$k_{c,t} = \frac{k_m}{4} \left[ \sqrt{\left(1 - V_f\right)^2 \left(\frac{k_{f,t}}{k_m} - 1\right)^2 + \frac{4k_{f,t}}{k_m}} - \left(1 - V_f\right) \left(\frac{k_{f,t}}{k_m} - 1\right) \right]^2 \quad (1)$$

where  $k_m$  and  $k_{f,t}$  are the thermal conductivity of the matrix (or air for dry reinforcements) and transverse thermal conductivity of fibers, respectively, and  $V_f$  is the fiber volume fraction. It must be said that a range of values have been reported for the transverse and axial thermal conductivity of carbon fibers, depending on precursor, manufacturing route, treatment and temperature [33]. Modeling becomes even more complicated for multilayer or woven fabrics, pointing to the necessity of measuring the thermal conductivity.

The main issue in the measurement of thermal conductivity is to account for the contact resistance [20]. Standardized Hukseflux THISYSTMTM and THASYSTMTM devices have been used for the measurements of the transverse and in-plane thermal conductivity, respectively [31]. They both include two samples sandwiched between a central thin heater and two outer heat sinks. A known heat flux is applied and temperature is measured at the heater and each heat sink: from these values and the dimensions of the samples, the thermal conductivity is determined according to Fourier's law. The contact resistance may be reduced by immersion in glycerol [31] but this would not be recommended for dry fabrics as the glycerol would infiltrate and loosen the fabric structure. In fact, as glycerol is still used for the rest of the contact surfaces, El-Hage et al. [33] sealed the dry fabric samples to avoid glycerol infiltration. They found that the through-thickness thermal conductivity of non-crimp carbon fabrics and twill woven carbon fabrics increased with increasing fiber fraction up to when a plateau was reached at about  $V_f = 0.43$  and  $0.50$ , respectively, which might be attributed to the corresponding increase in contact points and contact area up to the packing fraction. Beyond these studies [31,33], there have been no further developments in the technique for measuring the thermal conductivity of textiles in composite materials.

The use of infrared (IR) thermal mapping may be a better method to focus on the heat transfer inside the sample area only to determine its thermal conductivity and then move to the interface to determine the interface contact resistance. This novel technique has been recently developed in our group [34] to measure the thermal conductivity of a thermoelectric wearable textile and the individual materials of its composite structure. Hence, this latest novel technique will be investigated in this study to determine both the through-thickness transverse and in-plane conductivity of fabrics in this work, in particular with regard to the diaphragm forming process, as illustrated in Figure 1. The aim of this study is to determine the heat transfer properties of  $0/90^\circ$  biaxial fabrics of different architectures, including a non-crimp stitch bonded fabric, plain, twill and satin woven fabrics, and compare the values with the predictions of Clayton's model.

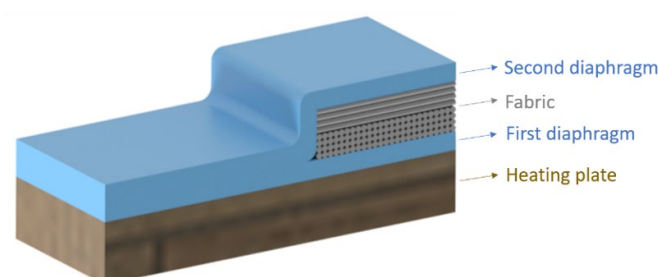


**Figure 1.** Schematic of cross-section of the heating plate and DDF assembly.

## 2. Materials and Methods

### 2.1. Materials

Figure 2 displays micrographs of the four fabrics tested in this study, where these images were obtained using a KEYENCE VHX-7000 digital microscope in transmission mode. A biaxial, non-crimp, 10 k carbon fiber fabric NCF300-biaxial (Figure 2a) of an areal density of  $300 \text{ g m}^{-2}$  and a measured uncompressed thickness of 0.70 mm. The NCF consisted of two identical plies at  $0/90^\circ$  orientation, held together with a polyester yarn in a straight plain stitch pattern with a pitch of 5 mm. A plain woven carbon fabric A0186/000 (Fothergill Engineered Fabrics, UK) (Figure 2b) with an areal density of  $199 \text{ g m}^{-2}$  and a measured uncompressed thickness of 0.27 mm. A  $4 \times 4$  twill woven 3 k carbon fabric A0188/000 (Fothergill Engineered Fabrics, UK) (Figure 2c) with 17 ends per inch and 17 picks per inch, an areal density of  $283 \text{ g m}^{-2}$ , and a measured uncompressed thickness of 0.31 mm. A 5H satin woven 3 k carbon fabric HexForce 433 (Hexcel, Stamford, CT, USA) (Figure 2d) with 18 ends per inch and 18 picks per inch, an areal density of  $285 \text{ g m}^{-2}$ , and a measured uncompressed thickness of 0.3 mm. A silicone rubber diaphragm was used in the simulated thermal conduction experiments (Figure 3a,b).

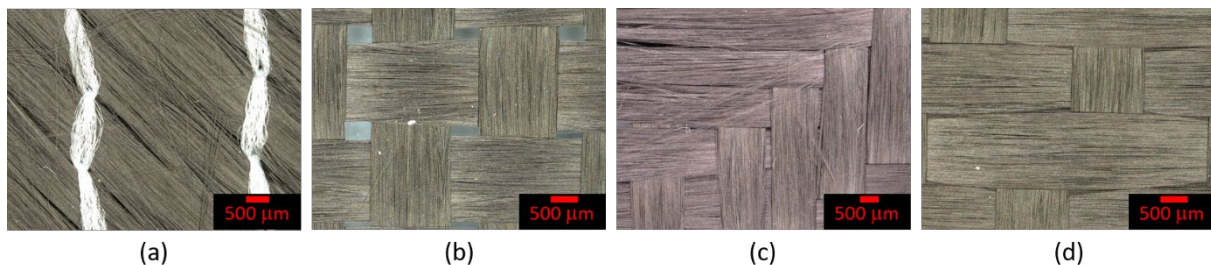


**Figure 2.** Micrographs of the tested four carbon fabrics: (a) NCF300-biaxial, (b) plain woven fabric, (c)  $4 \times 4$  twill woven fabric, and (d) 5H satin woven fabric.

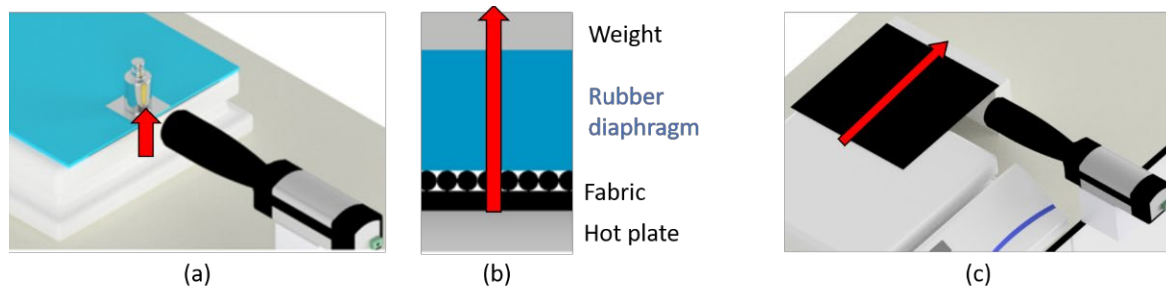


**Figure 3.** Diagrams of the setups for the measurement of (a) the transverse thermal conductivity and (c) the longitudinal thermal conductivity. The IR camera faces the fabric: (b) the assembly opposite the camera for the measurement of the transverse conductivity. Red arrows indicate the heat flow from the heated plate.

### 2.2. Measurement of the Specific Heat Capacity

The specific heat capacity of all the fabrics and the silicone rubber diaphragm was determined via differential scanning calorimetry (DSC) experiments, using a TA Instruments DSC Q1000. A DSC scan was carried out in the temperature range of  $15\text{--}140^\circ\text{C}$ , at a rate of  $5^\circ\text{C min}^{-1}$ .

### 2.3. Measurement of the Thermal Conductivity

The thermal diffusivity was determined from the analysis of temperature map videos captured using a thermal imaging IR camera, FLIR A300 with a high magnification lens ( $25 \mu\text{m}$  resolution). Figure 3 displays the two set ups for the measurement of the transverse (through-thickness) and longitudinal (one of the in-plane directions) thermal diffusivity. For

the measurement of the transverse diffusivity, the fabric was placed on the hot plate (Fisher Scientific 280 mm × 280 mm Digital Hotplate), covered by the silicone rubber diaphragm and secured in place using a weight on the top (Figure 3a,b). The camera faced the free thin side of the fabric as shown in Figure 3a. For the measurement of the longitudinal thermal diffusivity, the fabric was partly placed on the hot plate and was partly left “hanging” out of the plate as in a cantilever plate set up, with a thin support at the end so the fabric would remain flat during the experiment. The camera faced the free thin side of the fabric between the hot plate and the support.

Initially, the hot plate was at room temperature when the materials were assembled on top of it. To setup the camera and find the correct focus point, a piece of paper was used to not preheat any of the materials. The location was then marked so the fabric could be placed onto the hot plate in the correct position and was not preheated before the experiment began. During the experiment, the hot plate was heated from room temperature,  $T_{room} = 20\text{ }^{\circ}\text{C}$ , to  $100\text{ }^{\circ}\text{C}$ , mimicking the conditions in preforming where heating to  $90\text{--}100\text{ }^{\circ}\text{C}$  is required to activate the binder. The temperature images from the IR camera were video recorded at a frame rate of 30 Hz. All post-processing was carried out using the FLIR Tools+ software. The hot plate temperature was monitored using type-K thermocouples and recorded on a PICO thermocouple datalogger. For each type of fabric and conductivity measurement, 2–3 repeat experiments were carried out. The following heat transfer equation was applied for the fabric face opposite the camera:

$$\frac{\partial T}{\partial t} = \frac{k_i}{\rho c_p} \frac{\partial^2 T}{\partial x_i^2} + \frac{h}{\rho c_p l} (T_a - T) \tag{2}$$

where  $T$  is temperature,  $T_a$  is the ambient temperature,  $t$  is time,  $x_i$  is the dominant direction of heat flow, the transverse direction  $x_T$  for Figure 3a,b to measure the through-thickness transverse conductivity  $k_T$ , and the longitudinal direction  $x_l$  for Figure 3c to measure the longitudinal conductivity  $k_l$ .  $\rho$  is the fabric density, calculated from the areal density of fabric,  $\rho_a$ , divided by the fabric thickness as measured during the experiment with a micrometer and the IR camera photographs. While it is expected that the fabric is uncompressed in the measurement of the longitudinal conductivity, it is compressed in the measurement of the transverse conductivity. The fabric volume fraction is also calculated from its density, considering that it consists of carbon fiber (ignoring the stitch and binder mass) of a density of  $1760\text{ kg m}^{-3}$ .  $c_p$  is the specific heat capacity of the fabric measured from the DSC experiments.  $h$  is the heat transfer coefficient between the fabric and the air and  $l$  is the boundary layer length of this heat transfer due to natural convection.

Equation (2) is discretized following the time implicit finite volume/finite difference technique [34–36] yielding:

$$\frac{T_j^{n+1} - T_j^n}{\Delta t} = \frac{k_i}{\rho c_p} \frac{1}{(x_{i,j+1/2} - x_{i,j-1/2})} \left( \frac{T_{j+1}^{n+1} - T_j^{n+1}}{x_{i,j+1} - x_{i,j}} - \frac{T_j^{n+1} - T_{j-1}^{n+1}}{x_{i,j} - x_{i,j-1}} \right) + \frac{h}{\rho c_p l} (T_a - T_j^{n+1}) \tag{3}$$

where superscripts  $n$  and  $n + 1$  are the previous and current times,  $\Delta t$  is the timestep between  $n + 1$  and  $n$  times, and subscripts  $j - 1, j, j + 1$  (or their midpoints  $j + 1/2, j - 1/2$ ) denote successive discrete points in the  $x_i$  axis or the variable  $T$  at those locations. In general, triads of points were selected in the transverse direction (through-thickness) within the fabric and the silicone rubber diaphragm, as depicted in Figure 4a, or in the longitudinal direction, as depicted in Figure 4b, in images of temperature maps to use Equation (3) at different times in the temperature map video obtained from the IR thermal camera. The temperatures at these points were obtained, so an X-Y plot was constructed according to Equation (3):

$$Y = \frac{T_j^{n+1} - T_j^n}{\Delta t}, \rightarrow X = \frac{1}{(x_{i,j+1/2} - x_{i,j-1/2})} \left( \frac{T_{j+1}^{n+1} - T_j^{n+1}}{x_{i,j+1} - x_{i,j}} - \frac{T_j^{n+1} - T_{j-1}^{n+1}}{x_{i,j} - x_{i,j-1}} \right) \tag{3a}$$

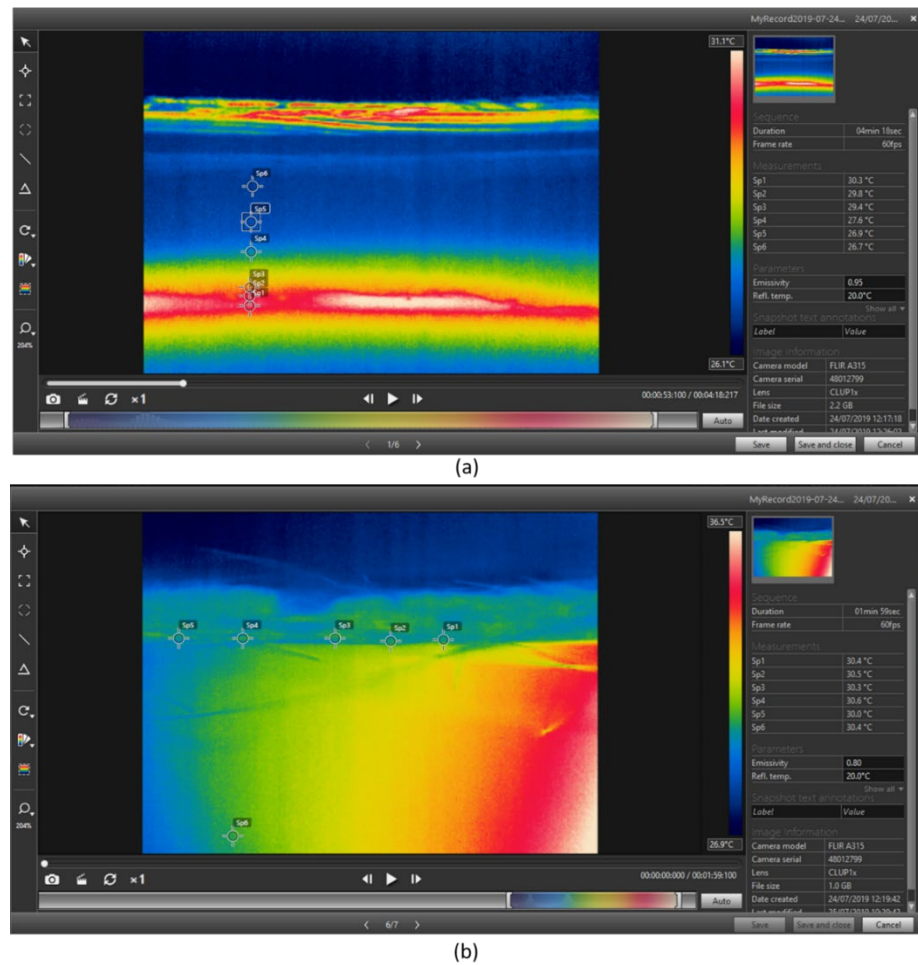


**Figure 4.** Examples of temperature maps and selected points for the determination of (a) the transverse thermal conductivity and (b) the longitudinal thermal conductivity.

Then, Equation (3) was linearly fitted to obtain the thermal diffusivity  $k_i/\rho c_p$  from the gradient of the line, where a constant rate of heat loss to the ambient environment was assumed represented by the intercept of the linear fit. Using the  $c_p$  value obtained from the DSC experiments, the transverse and longitudinal thermal conductivities were determined from the transverse and longitudinal thermal diffusivities, respectively. According to the discretization method in Equation (3), the method of determining the thermal diffusivity (and hence thermal conductivity) is second-order accurate with regard to the space interval between two consequent points in each triad of points  $j - 1, j, j + 1$  selected for the numerical analysis.

### 3. Results and Discussion

#### 3.1. Results of Specific Heat Capacity

Figures 5 and 6 present the results of the DSC experiments in the form of specific heat capacity,  $c_p$ , as a function of temperature. The results clearly show an almost linear relationship of the specific heat capacity as a function of temperature for most parts of each curve. The dip at the end of the  $c_p$  graphs indicates the end of the test a little before 140 °C. The silicone rubber seems to have the highest  $c_p$  value, varying from 1.3 J g<sup>-1</sup> K<sup>-1</sup> at 30 °C to 1.4 J g<sup>-1</sup> K<sup>-1</sup> at 138 °C (Figure 5a), which agrees with the literature [37] reporting  $c_p = 1.3$  J g<sup>-1</sup> K<sup>-1</sup> at room temperature for a silicon rubber of density 1100 kg m<sup>-3</sup>. The unidirectional NCF exhibits the lowest  $c_p$ , varying from 0.12 J g<sup>-1</sup> K<sup>-1</sup> at 30 °C to 0.25 J g<sup>-1</sup> K<sup>-1</sup> at 138 °C (Figure 5b). This agrees with the measured low  $c_p$  value of 0.1 g<sup>-1</sup> K<sup>-1</sup> at room temperature for pure graphite [38]. As fabrics are formed in

biaxial stitched or woven structures, more air is incorporated in the structure of higher  $c_p = 1 \text{ J g}^{-1} \text{ K}^{-1}$  [39] than graphite, increasing the overall  $c_p$  value of the fabric. NCF300-biaxial has a  $c_p$  varying from  $0.67 \text{ J g}^{-1} \text{ K}^{-1}$  at  $30 \text{ }^\circ\text{C}$  to  $0.82 \text{ J g}^{-1} \text{ K}^{-1}$  at  $138 \text{ }^\circ\text{C}$  (Figure 5c). According to the material specifications, the polyester stitch has a glass transition of  $80 \text{ }^\circ\text{C}$  and melting point of  $260\text{--}270 \text{ }^\circ\text{C}$ , and the binding agent has a melting point of  $110 \text{ }^\circ\text{C}$ . No endothermic effects indicating glass transition of the stitch or melting of the binder are visible in the DSC curves, which may be due to the fact that the amount of binder (below 5 wt%) and stitch in the sample pan on the DSC instrument are negligible in their effect on heat flow.

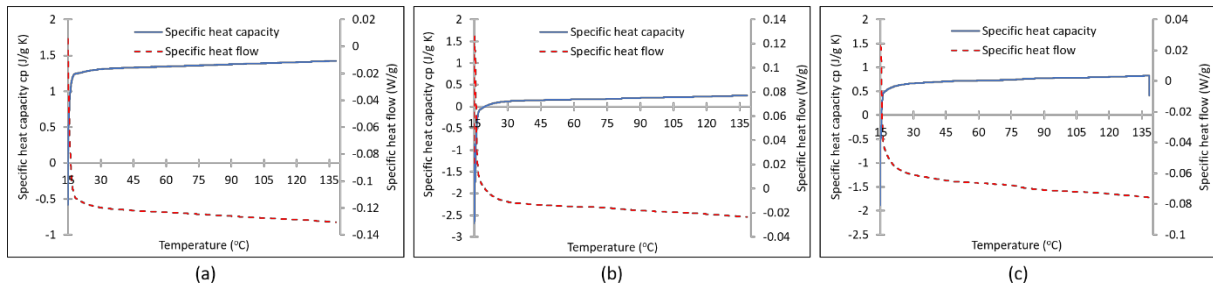


**Figure 5.** Results of the specific heat capacity from DSC experiments of (a) silicone rubber diaphragm, (b) NCF300-unidirectional, and (c) NCF300-biaxial.

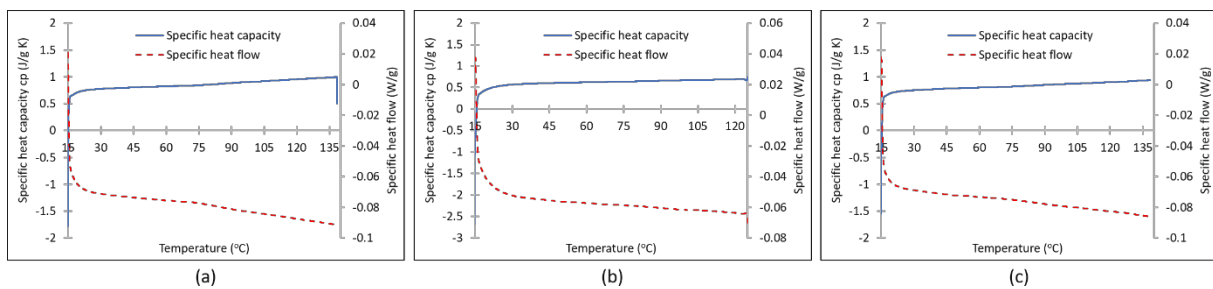


**Figure 6.** Results of the specific heat capacity from DSC experiments of (a) plain woven fabric, (b)  $4 \times 4$  twill woven fabric, and (c) 5H satin woven fabric.

The plain weave has a  $c_p$  varying from  $0.78 \text{ J g}^{-1} \text{ K}^{-1}$  at  $30 \text{ }^\circ\text{C}$  to  $1 \text{ J g}^{-1} \text{ K}^{-1}$  at  $138 \text{ }^\circ\text{C}$  (Figure 6a). The  $4 \times 4$  twill weave has a  $c_p$  varying from  $0.57 \text{ J g}^{-1} \text{ K}^{-1}$  at  $30 \text{ }^\circ\text{C}$  to  $0.7 \text{ J g}^{-1} \text{ K}^{-1}$  at  $125 \text{ }^\circ\text{C}$  (Figure 6b). The 5H satin weave has a  $c_p$  varying from  $0.75 \text{ J g}^{-1} \text{ K}^{-1}$  at  $30 \text{ }^\circ\text{C}$  to  $0.94 \text{ J g}^{-1} \text{ K}^{-1}$  at  $138 \text{ }^\circ\text{C}$  (Figure 6c).

### 3.2. Results of Thermal Conductivity

All results of thermal conductivity are summarized in Table 1. First of all, the analysis for the longitudinal thermal conductivity parallel to the fibers of one layer of NCF300-biaxial is presented in Figure 7, with the X,Y axes of the plot defined by the relations in (3a). Triads of points were selected in the bottom ply as depicted in Figure 4b, where parallel horizontal fibers were facing the camera. The linear fit of Equation (3) in Figure 7 yields an elongational thermal diffusivity of  $6.8 \times 10^{-6} \text{ m}^2 \text{ s}^{-1}$ , which after substituting the density and specific heat capacity values yields a value for the elongational thermal conductivity of NCF300-biaxial:  $k_{ll} = 2.9 \pm 0.4 \text{ W m}^{-1} \text{ K}^{-1}$  (standard error calculated from three repeat experiments). Taking the value of the axial thermal conductivity of T-300 carbon fibers as  $k_{f,a} = 8.4 \text{ W m}^{-1} \text{ K}^{-1}$  [31,39–43] and a measured  $V_f = 0.35$  (via burn off tests), the rule of mixtures yields a theoretically calculated  $k_{ll} = 2.94 \text{ W m}^{-1} \text{ K}^{-1}$ , which is very close to the experimental value, also taking into account the experimental errors.

**Table 1.** Thermal conductivity values for all fabrics of this study determined from the analysis of the experimental data of thermal map videos and from theoretical models using Equation (1) and the rule of mixtures for the prediction of the transverse and elongational conductivity, respectively.

Thermal Conductivity (W m <sup>-1</sup> K <sup>-1</sup> )	NCF300-Biaxial	Plain Weave	4 × 4 Twill Weave	5H Satin Weave
<i>k<sub>T</sub></i> experimental	0.070 ± 0.007	0.05 ± 0.02	0.04 ± 0.02	0.004 ± 0.003
<i>k<sub>T</sub></i> theoretical	0.063	0.069	0.057	0.065
<i>k<sub>ll</sub></i> experimental	2.9 ± 0.4			
<i>k<sub>ll</sub></i> theoretical	2.94			

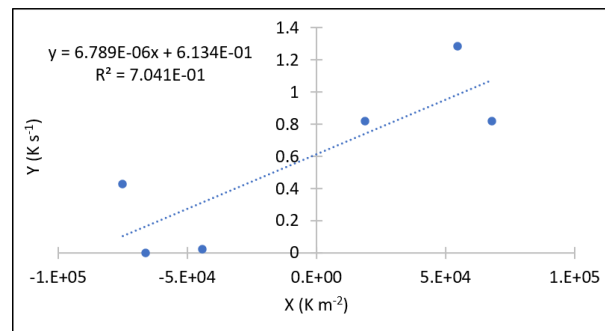


**Figure 7.** Results of the longitudinal thermal diffusivity (gradient of the linear equation) along the fiber direction of one ply for NCF300-biaxial. The X,Y axes of the plot are defined by the relations in (3a).

The next step is the determination of the transverse conductivity for all fabrics, the analysis of which is presented in Figure 8 and the results are presented in Table 1. Starting with NCF300-biaxial in Figure 8a, a transverse thermal diffusivity of  $0.15 \times 10^{-6} \text{ m}^2 \text{ s}^{-1}$  is determined from the gradient of the linear data fit, yielding a thermal conductivity of  $k_T = 70 \pm 7 \text{ mW m}^{-1} \text{ K}^{-1}$  (standard error calculated from three repeat experiments). Employing Clayton’s Equation (1) and substituting the values  $k_{f,a} = 8.4 \text{ W m}^{-1} \text{ K}^{-1}$  [31,39–43],  $k_{f,t} = 0.84 \text{ W m}^{-1} \text{ K}^{-1}$  [31,40,44], and air as the matrix with  $k_m = 26\text{–}34 \text{ W m}^{-1} \text{ K}^{-1}$  in the temperature range of 30–140 °C [45], the theoretical value for the transverse conductivity of NCF300-biaxial was found to be:  $k_T = 63 \text{ mW m}^{-1} \text{ K}^{-1}$ . Comparing our thermal conductivity values to those of El-Hage et al. [33], our elongational conductivity is lower, but ours refers to one ply with fibers parallel to the face opposite the thermal camera. Considering that our total NCF300-biaxial is at 0/90 orientation, the overall in-plane conductivity is the average of  $k_{ll}$  and  $k_T$  values (uncompressed), yielding  $1.45 \text{ W m}^{-1} \text{ K}^{-1}$ , which is similar to that measured in the literature [33]. Our  $k_T$  values are lower than El-Hage’s et al. [33], where the latter found  $k_T = 0.11 \text{ W m}^{-1} \text{ K}^{-1}$  for a six-layer NCF stack, but are closer to the theoretical values of Clayton’s model than El-Hage’s values. Furthermore, differences exist between NCFs with regard to the frequency and type of stitch, resulting in different size voids or eyelets at the locations of the stitch entering the fabric.

Figure 8b presents the analysis for yielding the transverse thermal conductivity of the plain weave in this study determined as  $k_T = 0.05 \pm 0.02 \text{ W m}^{-1} \text{ K}^{-1}$  (standard error calculated from two repeat experiments), which is lower than that of the NCF300-biaxial and lower than the prediction of Clayton’s model presented in Table 1 for an equivalent 0/90 ° fabric with the same fiber fraction as the plain weave,  $V_f = 0.42$ . It is clear that the large voids present at the yarn crossover points of the uncompressed plain weave (with such low  $V_f$ ) result in low transverse thermal conductivity and create a gap between the experimental and theoretical values. Moreover, a large data scatter in relation to the linear fit is observed in Figure 8b compared to Figures 8a and 7 and a high experimental error between the repeat experiments is also observed. This scatter was also observed in the measurements of the thermal conductivity of thermoelectric fabrics using thermal maps [34] and attributed to the fact that the  $j - 1, j,$  and  $j + 1$  numerical location points of the discretized Equation (3) were distributed in the mesoscopic scale of the fabric [46],

hence, each point may be located in a macropore between yarns or inside a yarn or at other intermediate locations. So, the individual temperature measurements do not represent the composite cross-section as a continuum but individual components of the mesoscopic structure. Nevertheless, it is considered that the best fits through each dataset represent an average thermal conductivity for the continuum.

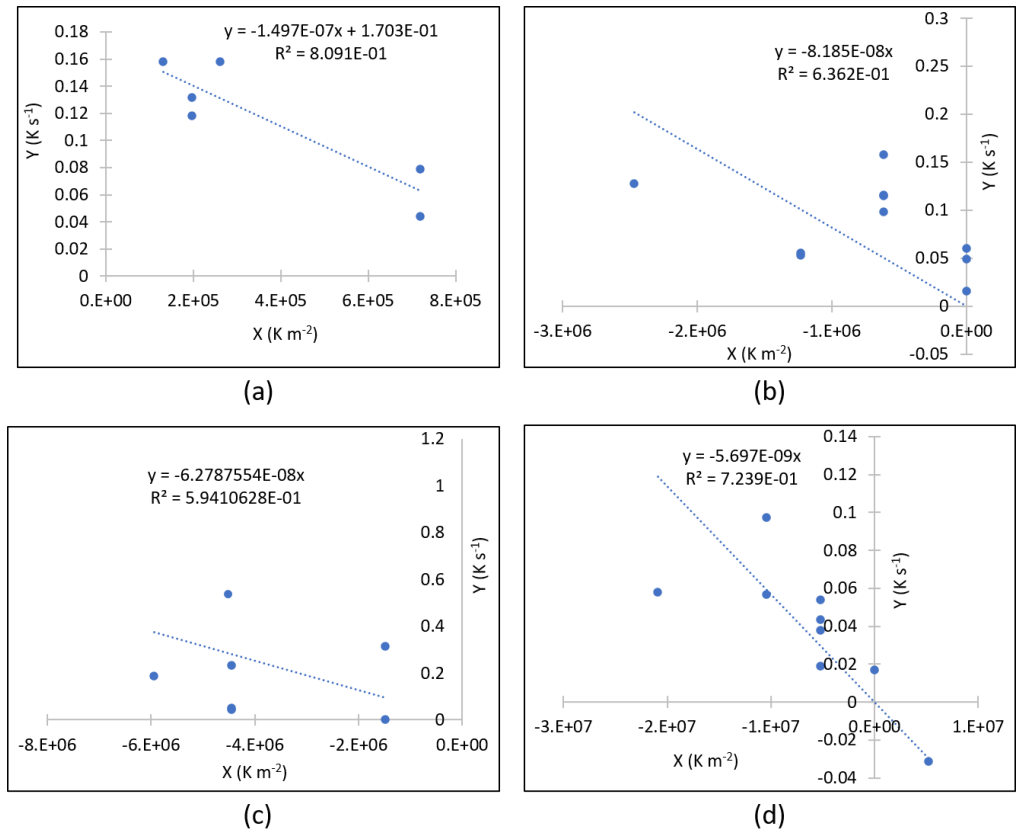


**Figure 8.** Results of the transverse thermal diffusivity (gradient of the linear equation) for one ply of (a) NCF300-biaxial, (b) plain woven fabric, (c) 4 × 4 twill woven fabric, and (d) 5H satin woven fabric. The X,Y axes of the plot are defined by the relations in (3a).

Figure 8c presents the analysis for the 4 × 4 twill weave resulting in  $k_T = 0.04 \pm 0.02 \text{ W m}^{-1} \text{ K}^{-1}$  (standard error calculated from two repeat experiments), which is similar to the transverse thermal conductivity of the plain weave, given similar issues of void space in the loose crossover regions. It is also compared to a higher theoretical value of  $k_T = 0.057 \text{ W m}^{-1} \text{ K}^{-1}$  for the 4 × 4 twill weave using Clayton’s model (Table 1), the difference again being due to the lack of a detailed microstructural pattern in Clayton’s model. The 5H satin weave (Figure 8d) had a surprisingly low transverse conductivity from the analysis of the temperature maps,  $k_T = 0.004 \pm 0.003 \text{ W m}^{-1} \text{ K}^{-1}$  (standard error calculated from two repeat experiments), which was confirmed from the analysis of the data from other triads of transverse locations in the fabric. The reason for this might be that the crossover pattern creates a much looser structure than an equivalent stitched fabric. In the case of the 5H satin weave, it seems that the long 0° yarn regions over four 90° yarns leave a long gap from the hot plate, which dramatically reduces the rate of heat conduction and, hence, the transverse thermal conductivity of the overall fabric.

It must also be noted that the heat conduction measurements were performed on a single layer of each fabric, in direct contact with the flat hot plate and the flat diaphragm, which leaves larger gaps compared to large stacks of fabrics which would benefit from the nesting of yarns and other microstructural features that would increase the overall number of contact points and contact area between individual fabric layers, yielding higher values

of transverse thermal conductivity. Indeed, this was observed by El-Hage et al. [33] when they increased the number of fabric layers in the stack, especially when they secured the assembly with through-thickness stitching in 3D fabric architectures.

#### 4. Conclusions

The heat transfer properties of single ply fabrics were measured using DSC to determine the specific heat capacity and temperature maps from the video of an IR thermal imaging camera to determine the longitudinal (parallel to fiber) and transverse (through-thickness of fabric) thermal conductivity. DSC in the temperature range of 30–138 °C yielded  $c_p$  values in the corresponding range of 1.3–1.4 J g<sup>-1</sup> K<sup>-1</sup> for silicone rubber (used as diaphragm material in preforming) and 0.12–0.25 J g<sup>-1</sup> K<sup>-1</sup> for the unidirectional carbon NCF, agreeing with the data in the literature [37,38]. Biaxial carbon woven fabrics exhibited higher  $c_p$  values than the unidirectional NCF, in the corresponding range of 0.67–0.82 J g<sup>-1</sup> K<sup>-1</sup> for the NCF300-biaxial, 0.78–1 J g<sup>-1</sup> K<sup>-1</sup> for the plain weave, 0.57–0.7 J g<sup>-1</sup> K<sup>-1</sup> for the 4 × 4 twill weave, and 0.75–0.94 J g<sup>-1</sup> K<sup>-1</sup> for the 5H satin weave.

One may conclude that the novel technique of thermal map analysis is appropriate for the determination of the thermal diffusivity at the continuum level from the linear fit of the experimental data, even if there is considerable data scatter due to the discrete locations of the data points distributed in the mesoscopic scale of the fabric architecture where individual points might correspond to voids or particular features of the yarn or tow pattern. In particular, the determined value of the elongational thermal conductivity  $k_{ll} = 2.9 \pm 0.4 \text{ W m}^{-1}\text{K}^{-1}$  of the NCF300-biaxial carbon fabric agreed well with the theoretical value calculated employing the rule of mixtures. The transverse thermal conductivity of the NCF300-biaxial carbon fabric is  $k_T = 0.070 \pm 0.007 \text{ W m}^{-1}\text{K}^{-1}$ , 41 times lower than the elongational thermal conductivity following the same trend as the predictions of the theoretical modeling, where the Clayton model was employed for  $k_T$ .

Comparing the different fabric architectures, the effect of voids due to yarn crossovers in woven fabrics was evident in the measured values of both  $c_p$  and  $k_T$ . A unidirectional NCF fabric exhibited the lowest  $c_p$  value, close to that of pure graphite. The rest of the biaxial fabrics, NCF or woven, had higher  $c_p$  values due to the air trapped in the voids of their structure. In terms of the measured transverse conductivity, all biaxial carbon fabrics, especially the woven fabrics that have more voids due to the yarn crossover regions, exhibited low thermal conductivity:  $0.05 \pm 0.02 \text{ W m}^{-1}\text{K}^{-1}$  for the plain weave,  $0.04 \pm 0.02 \text{ W m}^{-1}\text{K}^{-1}$  for the 4 × 4 twill weave, and  $0.004 \pm 0.003 \text{ W m}^{-1}\text{K}^{-1}$  for the 5H satin weave. This was attributed to the fact that they were all laid as single ply leaving large gaps between the fabric and the hot plate at or between the yarn crossover regions. It is also noticed that the percentage standard error in the repeat experiments to determine the transverse thermal conductivity is higher for the woven fabrics, 40–75%, than for the NCF-biaxial fabric, 10%. It is expected that stacks of fabrics would have higher transverse conductivity due to beneficial contributions from nesting effects. The Clayton model predictions of  $k_T$  demonstrated the best agreement for the NCF300-biaxial fabric which contained the smallest number of voids under compression, especially between the flat surfaces of the hot plate and the rubber diaphragm.

**Author Contributions:** Conceptualization, P.K. and C.L.; methodology, P.K. and C.L.; validation, P.K., C.L. and S.B.; formal analysis, P.K.; investigation, P.K., C.L. and S.B.; resources, C.L. and S.B.; data curation, P.K. and C.L.; writing—original draft preparation, P.K.; writing—review and editing, P.K. and C.L.; visualization, P.K.; supervision, C.L. and S.B.; funding acquisition, C.L. and S.B. All authors have read and agreed to the published version of the manuscript.

**Funding:** We gratefully acknowledge the funding of this project by EPSRC under the umbrella of the EngD programme MinMaT at the University of Surrey and industrial funding by McLaren Automotive Ltd.

**Data Availability Statement:** Data will be made available after reasonable requests to the corresponding authors.

**Acknowledgments:** The authors would also like to thank Violeta Doukova, Department of Physics, University of Surrey, for the DSC experiments.

**Conflicts of Interest:** The authors declare no conflict of interest.

## References

1. Moll, P.; Ohlberg, L.; Salzer, S.; Coutandin, S.; Fleischer, J. Integrated gripping-system for heating and preforming of thermoplastic unidirectional tape laminates. *Procedia CIRP* **2019**, *85*, 266–271. [[CrossRef](#)]
2. Brody, J.C.; Gillespie, J.W. The effects of a thermoplastic polyester preform binder on vinyl ester resin. *J. Thermoplast. Comp. Mat.* **2005**, *18*, 157–179. [[CrossRef](#)]
3. Yoo, H.M.; Lee, J.W.; Kim, J.S.; Um, M.K. Influence of non-reactive epoxy binder on the permeability and friction coefficient of twill-woven carbon fabric in the liquid composite molding process. *Appl. Sci.* **2020**, *10*, 7039. [[CrossRef](#)]
4. Schmidt, S.; Mahrholz, T.; Kühn, A.; Wierach, P. Powder binders used for the manufacturing of wind turbine rotor blades. Part 1. Characterization of resin-binder interaction and preform properties. *Polym. Compos.* **2018**, *39*, 708–717. [[CrossRef](#)]
5. Kappel, E.; Albrecht, M. A controlled recipient evacuation process to form composite profiles from flat multi-angle prepreg stacks—infrastructure and C-profile verification. *Adv. Manuf. Polym. Comp. Sci.* **2019**, *5*, 140–154. [[CrossRef](#)]
6. Chen, S.; McGregor, O.P.L.; Endruweit, A.; Elsmore, M.T.; De Focatiis, D.S.A.; Harper, L.T.; Warrior, N.A. Double diaphragm forming simulation for complex composite structures. *Compos. A Appl. Sci. Manuf.* **2017**, *95*, 346–358. [[CrossRef](#)]
7. Sun, J.; Gu, Y.; Li, M.; Ma, X.; Zhang, Z. Effect of forming temperature on the quality of hot diaphragm formed C-shaped thermosetting composite laminates. *J. Reinf. Plast. Comp.* **2012**, *31*, 1074–1087. [[CrossRef](#)]
8. Wakeman, M.; Rudd, C.D. Compression moulding of glass and polypropylene composites for optimised macro- and micro-mechanical properties—1 Commingled glass and polypropylene. *Comp. Sci. Technol.* **1998**, *58*, 1879–1898. [[CrossRef](#)]
9. Bader, M.G.; Lekakou, C. Processing for laminated structures. In *Composites Engineering Handbook*; Mallick, P.K., Ed.; CRC Press: Boca Raton, FL, USA, 1997; pp. 371–479.
10. Rutt, M.; Lekakou, C.; Smith, P.A.; Sordon, A.; Santoni, C.; Meeks, G.; Hamerton, I. Methods for process-related resin selection and optimisation in high-pressure resin transfer moulding. *Mater. Sci. Technol.* **2019**, *35*, 327–335. [[CrossRef](#)]
11. Liu, B.; Bickerton, S.; Advani, S.G. Modelling and simulation of resin transfer moulding (RTM)—gate control, venting and dry spot prediction. *Compos. A Appl. Sci. Manuf.* **1996**, *27*, 135–141. [[CrossRef](#)]
12. Xia, C.; Shi, S.Q.; Cai, L. Vacuum-assisted resin infusion (VARI) and hot pressing for CaCO<sub>3</sub> nanoparticle treated kenaf fiber reinforced composites. *Compos. B Eng.* **2015**, *78*, 138–143. [[CrossRef](#)]
13. Oromiehie, E.; Gangadhara Prusty, B.; Compston, P.; Rajan, G. Automated fibre placement based composite structures: Review on the defects, impacts and inspections techniques. *Compos. Struct.* **2019**, *224*, 110987. [[CrossRef](#)]
14. Lichtinger, R.; Hörmann, P.; Stelzl, D.; Hinterhölzl, R. The effects of heat input on adjacent paths during Automated Fibre Placement. *Compos. A Appl. Sci. Manuf.* **2015**, *68*, 387–397. [[CrossRef](#)]
15. Tafreshi, O.A.; Van Hoa, S.; Shadmehri, F.; Hoang, D.M.; Rosca, D. Heat transfer analysis of automated fiber placement of thermoplastic composites using a hot gas torch. *Adv. Manuf. Polym. Comp. Sci.* **2019**, *5*, 206–223. [[CrossRef](#)]
16. Nardi, D.; Sinke, J. Design analysis for thermoforming of thermoplastic composites: Prediction and machine learning-based optimization. *Compos. C Open Access* **2021**, *5*, 100126. [[CrossRef](#)]
17. Längauer, M.; Zitzenbacher, G.; Burgstaller, C.; Hochenauer, C. Enhanced infrared heating of thermoplastic composite sheets for thermoforming processes. *Int. Polym. Proc.* **2021**, *36*, 35–43. [[CrossRef](#)]
18. Babeau, A.; Comas-Cardona, S.; Binetruy, C.; Orange, G. Modeling of heat transfer and unsaturated flow in woven fiber reinforcements during direct injection-pultrusion process of thermoplastic composites. *Compos. A Appl. Sci. Manuf.* **2015**, *77*, 310–318. [[CrossRef](#)]
19. Liu, X.L.; Crouch, I.G.; Lam, Y.C. Simulation of heat transfer and cure in pultrusion with a general-purpose finite element package. *Compos. Sci. Technol.* **2000**, *60*, 857–864. [[CrossRef](#)]
20. Choo, H.L.; Martin, P.J.; Harkin-Jones, E.M.A. Measurement of heat transfer for thermoforming simulations. *Int. J. Mater. Form.* **2008**, *1*, 1027–1030. [[CrossRef](#)]
21. Tranchard, P.; Samyn, F.; Duquesne, S.; Estèbe, B.; Bourbigot, S. Modelling behaviour of a carbon epoxy composite exposed to fire: Part I—characterisation of thermophysical properties. *Materials* **2017**, *10*, 494. [[CrossRef](#)]
22. Bard, S.; Schön, F.; Demleitner, M.; Altstädt, V. Influence of fiber volume content on thermal conductivity in transverse and fiber direction of carbon fiber-reinforced epoxy laminates. *Materials* **2019**, *12*, 1084. [[CrossRef](#)] [[PubMed](#)]
23. Kinloch, I.A.; Suhr, J.; Lou, J.; Young, R.J.; Ajayan, P.M. Composites with carbon nanotubes and graphene: An outlook. *Science* **2018**, *362*, 547–553. [[CrossRef](#)] [[PubMed](#)]
24. Lei, C.; Lekakou, C. Activated carbon-carbon nanotube nanocomposite coatings for supercapacitor applications. *Surf. Coat. Technol.* **2013**, *232*, 326–330. [[CrossRef](#)]
25. Vermisoglou, E.C.; Giannakopoulou, T.; Romanos, G.; Boukos, N.; Psycharis, V.; Lei, C.; Lekakou, C.; Petridis, D.; Trapalis, C. Graphene-based materials via benzidine-assisted exfoliation and reduction of graphite oxide and their electrochemical properties. *Appl. Surf. Sci.* **2017**, *392*, 244–255. [[CrossRef](#)]

26. Muruges, A.K.; Uthayanan, A.; Lekakou, C. Electrophoresis and orientation of multiple wall carbon nanotubes in polymer solution. *Appl. Phys. A* **2010**, *100*, 135–144. [[CrossRef](#)]
27. Salifu, A.A.; Nury, B.D.; Lekakou, C. Electrospinning of nanocomposite fibrillar tubular and flat scaffolds with controlled fiber orientation. *Ann. Biomed. Eng.* **2011**, *39*, 2510–2520. [[CrossRef](#)]
28. Ashby, M.F. Chapter 11—Designing hybrid materials. In *Materials Selection in Mechanical Design*, 4th ed.; Elsevier: Amsterdam, The Netherlands, 2011; pp. 299–340.
29. Gibson, R.F. Micromechanics. In *Composites Engineering Handbook*; Mallick, P.K., Ed.; CRC Press: Boca Raton, FL, USA, 1997; pp. 167–202.
30. Paul, B. Prediction of elastic constants of multi-phase materials. *Trans. AIME* **1960**, *218*, 36–41.
31. Hind, S.; Robitaille, F. Measurement, modeling, and variability of thermal conductivity for structural polymer composites. *Polym. Compos.* **2010**, *31*, 847–857. [[CrossRef](#)]
32. Clayton, W.A. Constituent and composite thermal conductivities of phenolic-carbon and phenolic-graphite ablators. In Proceedings of the AIAA/ASME 12th Structures, Structural Dynamics and Materials Conference, Anaheim, CA, USA, 19–21 April 1971; pp. 1–17.
33. El-Hage, Y.; Hind, S.; Robitaille, F. Thermal conductivity of textile reinforcements for composites. *J. Text. Fibrous Mater.* **2018**, *1*, 1–12. [[CrossRef](#)]
34. Pope, J.; Lekakou, C. Thermoelectric polymer composite yarns and an energy harvesting wearable textile. *Smart Mater. Struct.* **2019**, *28*, 095006. [[CrossRef](#)]
35. Lekakou, C.N.; Richardson, S.M. Simulation of reacting flow during filling in reaction injection molding (RIM). *Polym. Eng. Sci.* **1986**, *26*, 1264–1275. [[CrossRef](#)]
36. Elsayed, Y.; Lekakou, C.; Tomlins, P. Modeling, simulations, and optimization of smooth muscle cell tissue engineering for the production of vascular grafts. *Biotechnol. Bioeng.* **2019**, *116*, 1509–1522. [[CrossRef](#)]
37. Keerthi Sagar, S.N.; Sreekumar, M. Miniaturized flexible flow pump using SMA actuator. *Procedia Eng.* **2013**, *64*, 896–906. [[CrossRef](#)]
38. Bastiurea, M.; Rodeanu Bastiurea, M.S.; Andrei, G.; Dima, D.; Murarescu, M.; Ripa, M.; Circiumaru, A. Determination of specific heat of polyester composite with graphene and graphite by differential scanning calorimetry. *Tribol. Ind.* **2014**, *36*, 419–427.
39. Carvill, J. 3-Thermodynamics and heat transfer. In *Mechanical Engineer's Handbook*; Elsevier: Amsterdam, The Netherlands, 1994; pp. 102–145.
40. Chamis, C.C. Simplified composite micromechanics equations for strength, fracture toughness and environmental effects. In Proceedings of the 39th Annual Conference, Reinforced Plastics/Composites Institute, New York, NY, USA, 16–19 January 1984; Society of Plastics Industry Inc.: Houston, TX, USA; pp. 1–16.
41. Klett, J.W.; Edie, D.D. Flexible towpreg for the fabrication of high thermal conductivity carbon/carbon composites. *Carbon* **1995**, *33*, 1485–1503. [[CrossRef](#)]
42. Ning, Q.G.; Chou, T.W. A closed-form solution of the transverse effective thermal conductivity of woven fabric composites. *J. Compos. Mater.* **1995**, *29*, 2280–2294. [[CrossRef](#)]
43. Gaier, J.R.; Yodervandenberg, Y.; Berkebile, S.; Stueben, H.; Balagadde, F. The electrical and thermal conductivity of woven pristine and intercalated graphite fiber-polymer composites. *Carbon* **2003**, *41*, 2187–2193. [[CrossRef](#)]
44. Dasgupta, A.; Agarwal, R.K.; Bhandarkar, S.M. Three-dimensional modeling of woven-fabric composites for effective thermo-mechanical and thermal properties. *Compos. Sci. Technol.* **1996**, *56*, 209–223. [[CrossRef](#)]
45. Air-Thermal Conductivity, vs. Temperature and Pressure. The Engineering ToolBox. Available online: [https://www.engineeringtoolbox.com/air-properties-viscosity-conductivity-heat-capacity-d\\_1509.html](https://www.engineeringtoolbox.com/air-properties-viscosity-conductivity-heat-capacity-d_1509.html) (accessed on 2 December 2021).
46. Amico, S.; Lekakou, C. Flow through a two-scale porosity, oriented fibre porous medium. *Transp. Porous Media* **2004**, *54*, 35–53. [[CrossRef](#)]